Energy Storage Materials 73 (2024) 103801

Contents lists available at ScienceDirect

Energy Storage Materials

journal homepage: www.elsevier.com/locate/ensm

Strong Lewis electron-pair bonding in vanadium oxide for ultra-fast and long-term stable Zn-ion storage

Siyuan Zhang [a], Leiming Lang [a,*], Yingjie Hu [a], Jianhua Sun [b], Guangxiang Liu [a], Guoqiang Luo [c], Linfeng Hu [d], Wenshu Chen [d,*]

[a] Jiangsu Key Laboratory of Zero-Carbon Energy Development and System Integration, Nanjing Xiaozhuang University, Nanjing, Jiangsu 211171, China
[b] School of Chemistry and Chemical Engineering and Institute of Advanced Functional Materials for Energy, Jiangsu University of Technology, Changzhou, Jiangsu 213001, China
[c] State Key Lab of Advanced Technology for Materials Synthesis and Processing, Wuhan University of Technology, Wuhan, Hubei 430070, China
[d] School of Materials Science and Engineering, Southeast University, Nanjing, Jiangsu 211102, China

ARTICLE INFO

Keywords:
Vanadium oxide
Phase transformation
Band structure engineering
Bond structure engineering
Ultra-fast and ultra-stable Zn^{2+} storage

ABSTRACT

Vanadium-based oxides typically show low electrical conductivity, high repulsion for Zn^{2+}, and severe structure collapse problems, resulting in unsatisfied cathode performance for aqueous Zn-ion batteries (AZIBs). Herein, we propose an advanced structural optimization strategy to address the above issues by constructing strong Lewis electron-pair bonding in vanadium oxide through initial doping Ca and a subsequent *in-situ* electrochemical activation process. We prepared the precursor of Ca-doped and amorphous carbon-encapsulated V_2O_3 material ($Ca_{0.17}V_2O_{3-x}$@C) and verified a phase transition into a layered V_2O_5-typed cathode during the activation process. Importantly, we find the initial-doped Ca and generated abundant oxygen vacancy defects are well restored in the phase-transformed crystal lattice. We reveal that band and bond structures of the phase-transformed cathode are optimized, exhibiting an improved electrical conductivity, optimal Zn^{2+} binding energy, ultra-low Zn-ion transport barrier, and considerably strong bonds of Ca-O and V-O, thereby realizing enhanced reaction kinetics and stability. The $Ca_{0.17}V_2O_{3-x}$@C exhibits surprisingly high-rate performance (233 mAh g^{-1} at 40 A g^{-1}) and excellent cycling stability (10,000 cycles with 82 % retention at 20 A g^{-1}). This work offers a novel and simple band and bond structure engineering strategy for preparing high-performance phase transformation typed vanadium oxide cathodes for AZIBs.

1. Introduction

Aqueous zinc-ion batteries (AZIBs) have become one of the most favorable substitutes for currently used lithium-ion batteries (LIBs) due to their abundant reserves, safety, and relatively high theoretical energy density [1–5]. At present, a great deal of research focuses on exploring promising cathode materials to pair with the Zn anode [6,7]. Vanadium-based oxides have been widely concerned because of their high specific capacity and varied structures [8]. Rhombohedral V_2O_3 has a typical open tunnel-shaped structure with a 3D framework of V-V chains. Thus, V_2O_3 can be efficiently inserted with ions, making it promising for AZIBs cathode [9]. In the case of two-electron redox, V_2O_3 will deliver a high theoretical capacity of 715 mAh g^{-1} (much higher than 589 mAh g^{-1} for V_2O_5) [10,11]. However, due to the low valence of vanadium, the original V_2O_3 crystal structure has strong electrostatic repulsion for Zn^{2+}, inevitably causing structural destruction during the initial activation process, thus reducing the structural toughness in subsequent cycles [12,13]. Besides, V_2O_3 itself is unstable (it tends to be oxidized to high-valence oxides) and has low electrical conductivity, further leading to poor rate performance and unstable cycling performance for AZIBs [14].

To address the above intractable problems, many effective strategies have been exploited to improve the electron/ion transport ability of V_2O_3 [15]. Composite with high conductive material is an effective approach to improve the electrical conductivity of the V_2O_3 cathode. Chen *et al.* synthesized V_2O_3@C nanospheres by coating dopamine on V_2O_5 followed by carbonization at a high temperature. Compared with the original V_2O_3, the carbon encapsulated V_2O_3@C sample has better electrical conductivity, exhibiting a good high-rate Zn^{2+} storage capacity of 321.7 mAh g^{-1} at 2 A g^{-1} [16]. Duan and co-workers prepared a

* Corresponding authors.
E-mail addresses: langleiming@njxzc.edu.cn (L. Lang), 101013800@seu.edu.cn (W. Chen).

https://doi.org/10.1016/j.ensm.2024.103801
Received 11 August 2024; Received in revised form 8 September 2024; Accepted 19 September 2024
Available online 20 September 2024

composite of V_2O_3@MXenes. The excellent conductivity of MXenes can accelerate the transport of Zn^{2+}. Therefore, the V_2O_3@MXenes cathode shows a superior rate performance (128 mA h g^{-1} at 60 A g^{-1}) [17]. In addition, It was reported that by constructing a hierarchical pore structure in cathodes, a high-speed channel for electron/ion transport could be provided, thereby improving the rate performance [18]. For example, Ding et al. prepared V_2O_3/C composite material with hierarchical pore structure by pyrolysis of V-MOFs, which exhibited a high reversible capacity of 350 mAh g^{-1} at 0.1 A g^{-1} and a considerable rate capacity of 250 mAh g^{-1} at 2 A g^{-1} [19].

There have also been many attempts to improve the structure stability of V_2O_3. Research shows that large pores can improve the toughness of the V_2O_3 structure, thereby improving the stability of the electrode during the charge and discharge process [20]. Park and co-workers prepared p-V_2O_3-CNT material composed of carbon nanotubes with large internal pore structures by spray pyrolysis process. The pore structure effectively alleviates the volume deformation during cycling and the p-V_2O_3-CNT cathode achieves a high retention of more than 83 % over 5000 cycles at 10 A g^{-1} [21]. Li et al. show that amorphous materials undergo small structure changes during the ion storage process, thereby improving the cycling stability. They prepared a nitrogen-doped amorphous vanadium oxide from V_2O_3 of N−V_2O_3@N−C *via* ammonia treatment and the cathode showed a high capacity retention of 96.4 % at 5 A g^{-1} after 1350 cycles [22]. Nevertheless, despite the above-employed methods, the current electrochemical zinc ion storage properties of vanadium oxides remain unsatisfactory, especially for the high-rate and long-term stability performance. There still lacks a favorable strategy to simultaneously enhance the electrical/ionic conductivity and stabilize the V-based skeleton of V_2O_3.

In this work, we propose a band and bond structure optimization strategy *via* forming strong Lewis electron-pair bonding in the crystal lattice to address the above issues for vanadium oxide cathode material. We utilized a doping (Ca) method to realize the proposed structure optimization. We prove the concept by preparing Ca-doped and carbon-encapsulated V_2O_3 material ($Ca_{0.17}V_2O_{3-x}$@C) and investigating the electrochemical Zn^{2+} storage properties and mechanism. We observed an *in-situ* electrochemical oxidation of $Ca_{0.17}V_2O_{3-x}$@C into a phase-transformed and stable compound with a layered V_2O_5-like structure upon the activation process of cycling. Importantly, we find out that the initial doped Ca and generated abundant oxygen vacancy defects are well restored in the phase-transformed crystal lattice during the long-term Zn^{2+}/H_3O^+ insertion and extraction process. The $Ca_{0.17}V_2O_{3-x}$@C shows greatly improved electrical conductivity, Zn-ion diffusion ability, and structure stability compared to those for the undoped V_2O_3, exhibiting quite promising electrochemical properties toward ultra-fast and long-term stable AZIBs. It delivers a remarkably high capacity of 426 mAh g^{-1} at 0.2 A g^{-1}, an exceptionally high energy density of 327 W h kg^{-1}, an excellent rate performance of 233 mAh g^{-1} at 40 A g^{-1}, and outstanding cycling stability of retention of 94 % after 2000 cycles at a moderate rate of 5 A g^{-1} and 245 mAh g^{-1} capacity remaining after 10,000 cycles at a high rate of 20 A g^{-1}. The $Ca_{0.17}V_2O_{3-x}$@C cathode material also demonstrates impressive potentials for pouch cell applications with high specific capacity and long cycling life. Experimental results and theoretical calculations reveal that the increased capacity and rate performance for the $Ca_{0.17}V_2O_{3-x}$@C originates from the optimized band structure induced by the Ca doping and generated abundant oxygen vacancy defects, which can improve the electrical conductivity and lower the diffusion barrier of Zn^{2+} during the energy storage process. The enhanced Zn^{2+} storage stability of $Ca_{0.17}V_2O_{3-x}$@C is mainly due to the optimized bond structure from the initial-doped Ca, which causes a considerably strong bond of Ca-O and improved bond strength of V-O in the phase-transformed compound. This work provides a simple and effective way of band and bond structure engineering for vanadium oxide-based cathodes towards high-performance AZIBs.

2. Experimental section

2.1. Preparations of the doped and undoped samples

The $Ca_{0.17}V_2O_{3-x}$@C material was prepared *via* a simple two-step process of mixing and calcination. Firstly, 4 mmol of vanadium pentoxide (V_2O_5) powders and 5 mL hydrogen peroxide (H_2O_2) were added to 40 mL deionized water (H_2O) followed by stirring to form solution A. Then, 4 mmol of calcium chloride ($CaCl_2$) and 4 mmol of glucose were added into 20 mL of deionized water followed by stirring to form solution B. After continuously stirring for 30 min, solution B was added drop wisely into solution A under stirring for 24 h to form an orange clear solution C. Subsequently, solution C was heated at 80 °C to evaporate water and obtain precursor. After that, the precursor was sintered at 700 °C for 1 h in an Ar atmosphere with a heating rate of 4 °C/min. When finished, the sintered products were washed several times with distilled water and ethanol followed by centrifugal collection and vacuum drying. The final product was collected and denoted as $Ca_{0.17}V_2O_{3-x}$@C. Other CaVO@C samples with various Ca and carbon contents were obtained by changing the initial addition amount of $CaCl_2$ (from 0 % to 100 %, in which the percentage is calculated as the mole ratio of Ca to V element) and glucose (from 0 % to 100 %, in which the percentage is calculated as the mole ratio of glucose to V element) using the same procedure. The $Ca_{0.17}V_2O_3$@C material was synthesized following the same steps except for changing the sintering atmosphere into air. The synthetic process of V_2O_{3-y}@C material is the same as that of $Ca_{0.17}V_2O_{3-x}$@C material with no calcium source.

2.2. Preparations of the doped and undoped sample cathodes

The electrochemical Zn^{2+} storage properties were evaluated by assembling CR2032 coin cell batteries. The cathodes were prepared by mixing the active material, super-P, and polyvinylidene fluoride (PVDF) in a weight ratio of 7:2:1 with the help of N-methyl-pyrrolidone (NMP) to form a homogeneous slurry. The slurry was then coated onto titanium foils, followed by vacuum drying at 80 °C overnight and cropping to get the cathode electrodes. The resulting mass loading of active material was controlled in the range of 1-2 mg cm^{-2}. Then the coin cells were assembled in the air by using prepared electrodes (diameter of 12 mm) as the cathode, zinc foil (thickness of 0.05 mm, diameter of 16 mm) as the anode, and 3 M aqueous $Zn(CF_3SO_3)_2$ solution as the electrolyte.

2.3. Fabrication of pouch cells

The Zn//$Ca_{0.17}V_2O_{3-x}$@C pouch cells were fabricated in air atmosphere. Firstly, a 0.5 × 2.0 cm blank part was reserved on the titanium foil (cathode current collector) and the zinc foil (anode) as the tab-leads. Then, the cathode ($Ca_{0.17}V_2O_{3-x}$@C coated on the titanium foil), glass fiber separator, and anode are fully immersed in the 3 M aqueous Zn $(CF_3SO_3)_2$ electrolyte and connected in a sandwich manner. Finally, the aluminum plastic film was utilized as the outer packaging material and heated in air for packaging. The working area for the Zn//$Ca_{0.17}V_2O_{3-x}$@C pouch cell was about 3 × 3 cm^2 with the active material mass loading of ca. 4.5 mg cm^{-2}.

2.4. Material characterizations

Scanning electron microscope (SEM) observations were performed on Tescan Mira 4 to investigate the morphology. Transmission electron microscopy (TEM), high-resolution transmission electron microscopy (HRTEM), and high-angle annular dark field-scanning transmission electron microscope (HADDF-STEM) images were conducted on JEOL JEM-F200. X-ray diffraction (XRD) spectra were characterized on Bruker D8 Advance using Cu Kα rays (λ = 0.15406 nm). X-ray photoelectron spectroscopy (XPS) data were collected on SHIMADZU AXIS ULTRA DLD with monochrome Al Kα X-ray beam (15 kV, 10 mA). Raman spectra

were recorded on HORIBA LabRAM HR Evolution with an excitation laser wavelength of 532 nm. Thermogravimetry (TG) analysis was tested on NETZSCH TG 209 F3 Tarsus in an air atmosphere with a heating rate of 5 °C/min. Electron paramagnetic resonance (EPR) was completed on Bruker EMXplus-6/1. Inductively coupled plasma optical emission spectrometry (ICP-OES) test was conducted on Agilent 7700.

2.5. Electrochemical measurements

All the assembled coin cells and pouch cells were rested for 24 h before any electrochemical performance test. Galvanostatic charge/discharge cycling was conducted on a NEWARE multichannel battery test system within the voltage window of 0.2 to 1.8 V (The specific capacity calculation is based on the total mass of the active material). Cycling Voltammetry (CV) and electrochemical impedance spectrometry (EIS) data were recorded on an electrochemical workstation (Bio-Logic VSP).

For the electrochemical Zn^{2+} storage stability test in Figs. 2, S14, and S15, we first activate the coin cell batteries by applying a small current density of 0.2 A g^{-1} for two cycles. Then the batteries start to run long-term cycles under set current densities.

2.6. Theoretical calculations

All calculations were carried out under the scheme of spin-polarized DFT using CASTEP [23]. Specifically, the Perdew-Burke-Ernzerhof (PBE) exchange-correlation function within the generalized gradient approximation was employed to describe the exchange-correlation energy [24]. Geometric convergence tolerances were set for the maximum force of 0.03 eV/A°, maximum energy change of 10^{-5} eV/atom, maximum displacement of 0.001 A°, and maximum stress of 0.5 GPa. The sampling in the Brillouin zone was set with 9 × 9 × 1 by the Monkhorst-Pack method.

The diffusion of Zn^{2+} ion was investigated by searching the possible diffusion route and identifying the migration transition state with the lowest diffusion energy barrier. The diffusion energy barrier is the energy difference between the total energies of the transition state and the initial structure. The transition state is searched by the generalized synchronous transit (LST/QST) method [25] implemented in the CASTEP code. The algorithm starts from a linear synchronous transit (LST) optimization and continues with a quadratic synchronous transit (QST) maximization process. Thereafter, the conjugate gradient (CG) minimization is conducted from the obtained LST/QST structure to refine the geometry of the transition state. The LST/QST/CG calculations are repeated till a stable transition state is obtained.

3. Results and discussion

We select calcium as the doping element with considerations of the following aspects: (i) the high-valanced Ca^{2+} can act as a strong Lewis acid and then form a strong Lewis electron-pair bonding with the strong Lewis base of O^{2-} in the vanadium oxide crystals. (ii) The large atomic

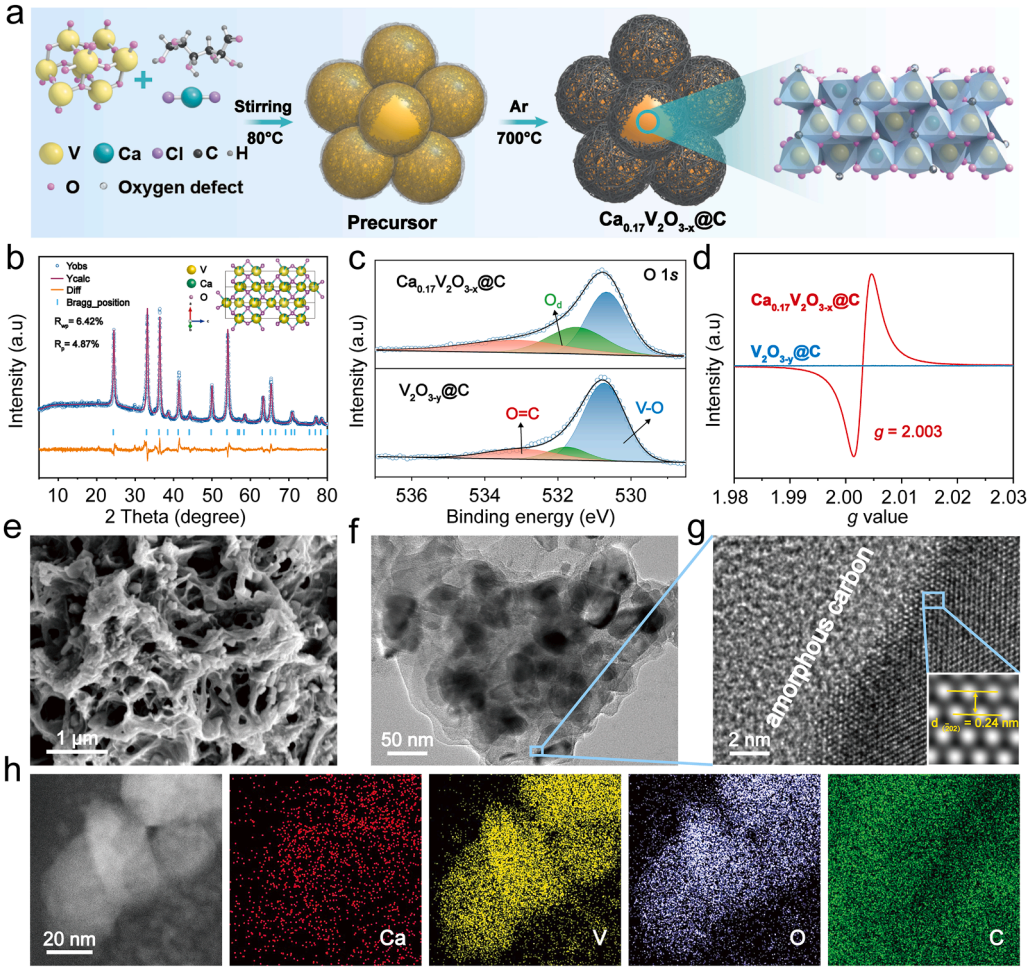

Fig. 1. Synthesis of $Ca_{0.17}V_2O_{3-x}$@C material. (a) A schematic of the synthetic route for $Ca_{0.17}V_2O_{3-x}$@C. (b) Rietveld-refined XRD pattern and a schematic of the crystal structure of $Ca_{0.17}V_2O_{3-x}$@C. (c) XPS spectra of O 1s and (d) EPR curves of $Ca_{0.17}V_2O_{3-x}$@C and V_2O_{3-y}@C samples, respectively. (e) SEM, (f) TEM, and (g) HRTEM images of $Ca_{0.17}V_2O_{3-x}$@C. (h) HADDF-STEM and corresponding elemental mapping results of $Ca_{0.17}V_2O_{3-x}$@C.

radius difference between Ca and O may induce a certain degree of structural distortion in the crystal after doping. A moderate crystal distortion can effectively alleviate the stress generated during the ion insertion process, thereby enhancing the structure stability. (iii) Doping can regulate electron energy levels, leading to improved electron conductivity. (iv) Doping can generate oxygen vacancy defects, which will increase the lattice active sites for Zn^{2+} storage and improve electron and ion conductivities [26].

The schematic synthetic route of $Ca_{0.17}V_2O_{3-x}$@C is briefly shown in Fig. 1a. Typically, $CaCl_2$ (dopant) and glucose (carbon source) were added into the V_2O_5 aqueous solution, followed by a simple two-step process of mixing and calcination (During the calcination process, the carbon source (C) acts as a reducing agent, reducing V_2O_5 to V_2O_3 under high temperature, the calcination reaction is $V_2O_5 + C \rightarrow_{Ar}^{700^{\circ}C} V_2O_3 + CO_2$), then we got the desired $Ca_{0.17}V_2O_{3-x}$@C materials. The synthetic details can be found in the experimental section. We find that after calcination, the original V_2O_5 transforms into V_2O_3 (Fig. S1). The successful synthesis of Ca-doped V_2O_3 materials can be verified from the X-ray diffraction (XRD) results (Fig. S1) that it has a 1.1° left shift for the (104) plane of V_2O_3, indicating a lattice distortion induced by the Ca doping into the V_2O_3 crystal. The success of Ca doping can also be identified from the Ca 2*p* orbital and full X-ray photoelectron spectroscopy (XPS) spectra, indicating the exitance of Ca dopant (Figs. S2 and S5). The position of doped Ca in the V_2O_3 crystals is derived by XRD and the subsequent Rietveld refinement, shown in Fig. 1b. Results show that $Ca_{0.17}V_2O_{3-x}$@C has a hexagonal structure with space group of *R3/c* and lattice parameters of $a = 4.9573(50)$ Å, $b = 4.9573(50)$ Å, $c = 14.0185(13)$ Å, $\alpha = \gamma = 90.0^{\circ}$, and $\beta = 120^{\circ}$. The satisfactory Rietveld refinement plot with acceptable reliability factors of $R_p = 4.87$ % and $R_{wp} = 6.42$ % suggests the high propensity for Ca to replace V atoms in the V_2O_3 lattice. The stoichiometric of Ca to V is about 1:13 (based on the inductively coupled plasma optical emission spectrometry (ICP-OES) results, see Table S1), thus we donate the synthesized compound of Ca-doped V_2O_3 as $Ca_{0.17}V_2O_{3-x}$@C.

By deconvoluting the XPS results of O 1*s* and V 2*p* orbitals for the synthesized samples, we find out that the Ca doping can generate abundant oxygen vacancy defects in the V_2O_3 crystal. In Fig. 1c, the XPS spectrum of O 1*s* orbital for $Ca_{0.17}V_2O_{3-x}$@C is deconvoluted into three peaks of 530.6, 531.5, and 533.2 eV, which correspond to the V-O bond, oxygen vacancy defect (O_d), and C=O bond, respectively. Carbonyl groups (C=O), which are attributed to coated carbon, can improve the hydrophilicity of the material, allowing the active substance to fully participate in the electrochemical reactions [27]. The oxygen vacancy defects can be identified from the comparison of the deconvolution results (Fig. S3) of O 1*s* orbitals of $Ca_{0.17}V_2O_{3-x}$@C and $Ca_{0.17}V_2O_3$@C, which is obtained by calcinating $Ca_{0.17}V_2O_{3-x}$@C in the air (Fig. S4, details can be found in the experimental section). Fig. S3 clearly shows that the oxygen vacancy defects can be repaired by oxygen-rich calcination, verifying the existence of oxygen vacancy defects in the prepared $Ca_{0.17}V_2O_{3-x}$@C material. The electron paramagnetic resonance (EPR) spectra in Fig. 1d further prove the oxygen vacancy defects in $Ca_{0.17}V_2O_{3-x}$@C. By contrast, the XPS results of O 1 *s* orbital (Fig. 1c) and EPR results (Figs. 1d and S6) clearly show that the incorporated Ca into V_2O_3 can yield a higher ratio of oxygen vacancy defects as compared to the undoped V_2O_3 sample (denoted as V_2O_{3-y}). The oxygen vacancy defects in undoped V_2O_3 may be generated from the inert oxygen-free Ar atmosphere during the calcination process. Therefore, we believe that the oxygen vacancy defects are mainly introduced by the calcium doping.

The scanning electron microscopy (SEM) image in Fig. 1e shows that the prepared $Ca_{0.17}V_2O_{3-x}$@C possesses a porous and interconnected microstructure. We further employ transmission electron microscopy (TEM) characterization to observe its nanostructure. As can be seen in Fig. 1f, the prepared $Ca_{0.17}V_2O_{3-x}$@C samples show a typical carbon-encapsulated structure with a domain crystal size of tens of nanometers. The clear lattice structure from high-resolution TEM (HRTEM) observation demonstrates the high crystallinity for the synthesized $Ca_{0.17}V_2O_{3-x}$@C material (Fig. 1g). Also, from Fig. 1g, it can be seen that the carbon layer is well integrated with the interface, which is beneficial for electron transport and improved stability. Compared to the undoped sample of V_2O_{3-x}@C, the doped sample of $Ca_{0.17}V_2O_{3-x}$@C shows higher electronic conductivity (Table S3). The TEM-coupled energy dispersive spectrometer (EDS) elemental mapping results of $Ca_{0.17}V_2O_{3-x}$@C distinctly show the even distribution of Ca, V, O, and C elements throughout the structure.

Raman spectrum was conducted to study the chemical structure of $Ca_{0.17}V_2O_{3-x}$@C. In Fig. S7, the low-frequency signals at 157 and 141 cm^{-1} can be interpreted as the stretching vibration mode of V=O, and the peaks located at 318, 858, 920, and 940 cm^{-1} can be attributed to various V-O bonds [28]. The signals at 1344 and 1598 cm^{-1} correspond to the D (defect or disordered) band and G (graphite and ordered) band of carbon (with a height ratio of D: G of 1.03) revealing the existence of a certain degree of conductive carbon layer for the synthesized $Ca_{0.17}V_2O_{3-x}$@C material. The carbon content is calculated to be about 12.7 wt.% from the thermogravimetric (TG) analysis (Fig. S8).

The electrochemical Zn^{2+} storage performance of prepared $Ca_{0.17}V_2O_{3-x}$@C cathode material was then studied by assembling coin cell-typed Zn//$Ca_{0.17}V_2O_{3-x}$@C batteries (details can be found in the experimental section). The voltage range was set to be 0.2–1.8 V. Fig. 2a shows the typical cyclic voltammetry (CV) profiles of the cells for 15 cycles at a scan rate of 0.1 mV s^{-1}. For the first cycle, a high and sharp oxidation peak appears at 1.4 V, while it disappears in the subsequent cycle, indicating a phase transition occurs upon the initial Zn^{2+} insertion process [29]. The oxidation peak in the first cycle of the CV curve corresponds to the oxidation transition from V^{3+} to V^{5+}. The reason for this transition is that as the voltage increases, the V-O bond is disrupted. Then the continuous dissociation of water leads to the disruption of the local pH and charge environment, resulting in subsequent structural rearrangement [30]. In Fig. S9, we have conducted the CV curve of pure V_2O_3, we also observed an oxidation peak in the first cycle and then disappears in subsequent cycles, confirming that irreversible phase transitions also occur in pure V_2O_3. After 15 cycles, the unchanged CV profiles indicate the electrochemical reactions become stable. *Ex-situ* XRD was used to explore the structure of the product after 15th full discharge and electrochemical stabilization (Fig. 2b). Some new diffraction peaks appear at 6.5°, 26°, and 34°, which can be indexed to diffractions from the (00*l*) planes of $Zn_{3.8}Ca_{0.16}V_2O_{5-x}{\cdot}nH_2O$ [31–33]. In addition, there are also some new peaks located at 13°, 19.6°, and 33°, which could be attributed to the presence of layered double hydroxide (LDH) of $Zn_x(OTF)_y(OH)_{2x-y}{\cdot}zH_2O$ [34,35]. The $Zn_x(OTF)_y(OH)_{2-x-y}{\cdot}zH_2O$ is formed by the reaction of OH^- in the electrolyte (produced by the decomposition of water) with $Zn(CF_3SO_3)_2$ and H_2O, which is commonly believed to be deposited at the cathode/electrolyte interface and acts as a breathing solid electrolyte interphase (SEI) [36–39]. Meanwhile, an equal amount of H^+ is produced, which will be inserted into the electrode together with Zn^{2+} to achieve electrical neutrality, known as the co-intercalating mechanism of Zn^{2+} and H^+, which has been reported previously [36]. Additionally, it can be seen that the diffraction peak of the (001) plane of the phase-transformed layered V_2O_5-type compound within initial Ca-doping shifts slightly compared with that of Ca-free (undoped) V_2O_{3-y} material, indicating the initial-doped Ca is restored after phase transition and electrochemical stabilization, thus causing lattice distortion (Fig. S10). Therefore, our *in-situ* electrochemical activation synthesis method differs from the conventional hydrothermal methods which utilize the metal ions as pillars [40,41]. Given the above experimental evidence, we have drawn a schematic of the phase transformation from the initial $Ca_{0.17}V_2O_{3-x}$@C into a phase-transformed and stable discharged compound of $Zn_{3.8}Ca_{0.16}V_2O_{5-x}{\cdot}nH_2O$ in Fig. 2c.

To further study the structural changes of $Ca_{0.17}V_2O_{3-x}$@C cathode after phase transition. and electrochemical stabilization, an *ex-situ* XPS

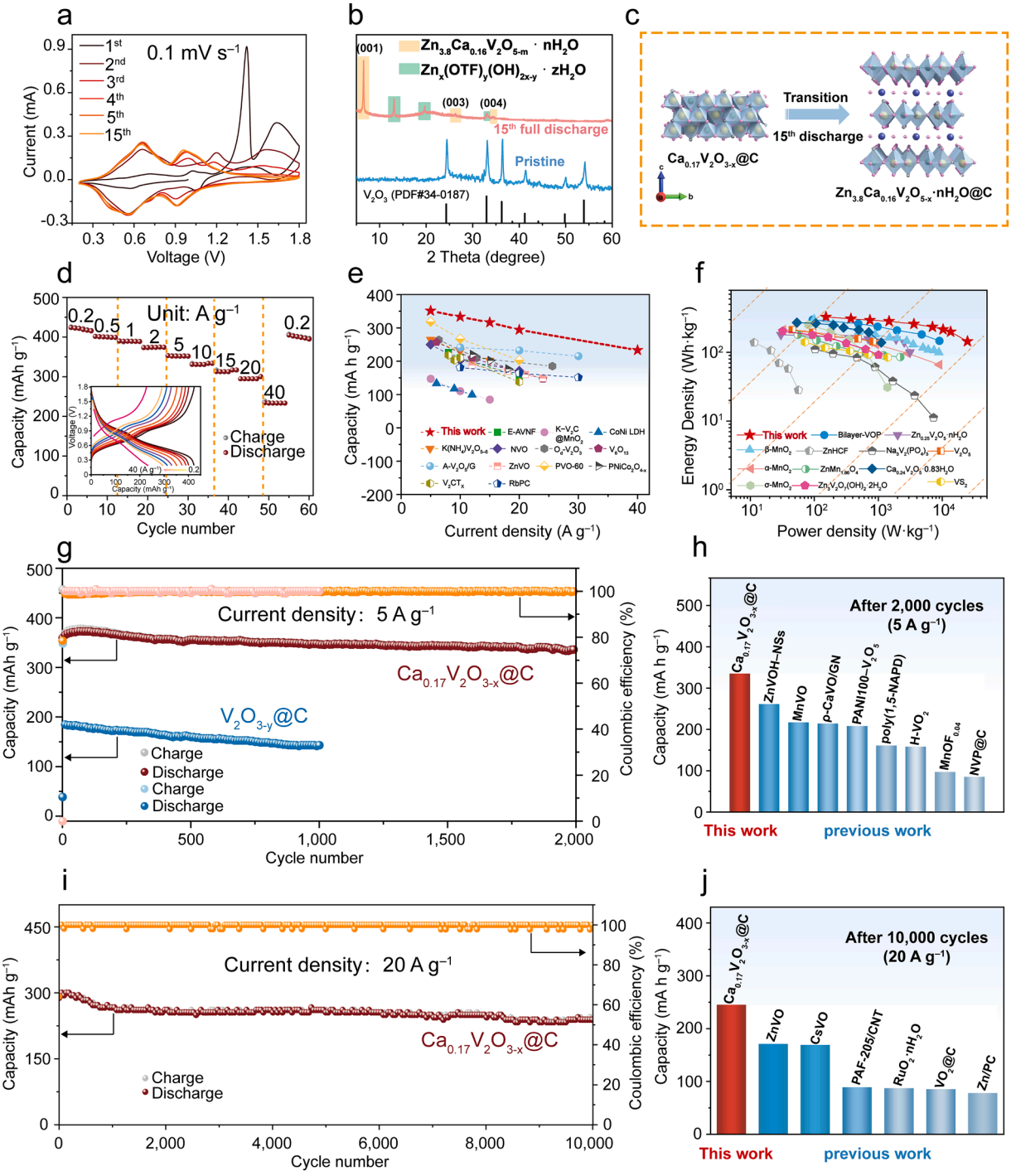

Fig. 2. Electrochemical Zn^{2+} storage performance of $Ca_{0.17}V_2O_{3-x}$@C material. (a) CV curves at 0.1 mV s^{-1}. (b) *Ex-situ* XRD patterns of $Ca_{0.17}V_2O_{3-x}$@C electrodes at pristine (no charge/discharge) and after the 15th full discharge (cut-off at 0.2 V). (c) A schematic of phase transformation of $Ca_{0.17}V_2O_{3-x}$@C cathode material after 15 cycles for electrochemical stabilization. (d) Rate performance at current densities ranging from 0.2 to 40 A g^{-1}. The inset shows the corresponding GCD curves. (e) A comparison of the rate performance of $Ca_{0.17}V_2O_{3-x}$@C material in this work and some recently reported representative AZIB cathodes [8,36,42–52]. (f) Ragone plots of $Ca_{0.17}V_2O_{3-x}$@C material in this work and some recently reported representative AZIB cathodes [32,53–63]. (g) Long-term cycling performance of $Ca_{0.17}V_2O_{3-x}$@C and V_2O_{3-x}@C at 5 A g^{-1}. (h) A comparison on the capacity after 2000 cycles (5 A g^{-1}) in this work and some reported representative AZIB cathodes [64–71]. (i) Long-term cycling performance of $Ca_{0.17}V_2O_{3-x}$@C at 20 A g^{-1}. (j) A comparison of the capacity after 10,000 cycles (20 A g^{-1}) in this work and some reported representative AZIB cathodes [36,72–76].

test was carried out on the sample under the condition of full discharge (i.e. cut-off at 0.2 V) after 15 cycles (Fig. S11). In Fig. S11a, we do not observe any reduction in the intensity of the Ca 2*p* signal after phase transition and electrochemical stabilization. The TEM-EDS elemental mapping results distinctly show that the Ca element still exists in the electrode after 2000 cycles (Fig. S12). These results confirm that the doped Ca^{2+} component is well restored during the electrochemical charge/discharge process, indicating the high stability of formed Ca-O bonds. We also notice a blue shift for the binding energies of the Ca^{2+} component after phase transition and electrochemical stabilization (346.2 eV for the pristine state and 347.6 eV for the discharged state at 0.2 V), which is attributed to the insertion of Zn^{2+}. During the discharge

process, the intercalation of a large number of Zn^{2+} led to changes in the charge environment and the structure surrounding Ca atoms, as well as changes in the binding energy of the inner shell electrons of Ca atoms, resulting in a significant blue shift in binding energy. Similar results can be found in $Ca_{0.25}V_2O_5{\cdot}xH_2O$ cathode [58], and Cr intercalated $CaCO_3$ material [77]. Further, it is worthwhile to note that after cycles, the full width at half maximum (FWHM) of the Ca 2*p* peak becomes larger compared with that of the initial $Ca_{0.17}V_2O_{3\text{-}x}$@C, which is believed to be caused by the generation of some oxygen vacancy defects in the electrode after phase transition [78]. After cycles, we can observe the Zn^{2+} 2*p* signal from Fig. S11b, confirming the fully discharged or fully absorbed/intercalated Zn^{2+} state at 0.2 V. Fig. S11c displays the comparison on V 2*p* spectra of $Ca_{0.17}V_2O_{3\text{-}x}$@C before and after cycles. The pristine electrode shows V^{3+} and V^{4+} components (V^{4+} is attributed to the oxidation of V^{3+} on the surface) [79]. Notably, a strong V^{5+} signal is observed at the fully discharged state, which results from the formation of the V_2O_5-type phase. The O 1*s* spectra shown in Fig. S11d demonstrate that oxygen vacancy defects are well retained in the fully discharged sample after 15 cycles This intercalation process is verified by the TEM analysis (Fig. S12). The chemical formula of $Zn_{3.8}Ca_{0.16}V_2O_{5\text{-}x}{\cdot}nH_2O$ after phase transition and electrochemical stabilization at 0.2 V is supported by HRTEM results (Fig. S12b) and ICP-OES result (Table S2).

To find out the optimal content of Ca dopant and coated carbon for efficient Zn^{2+} storage, we prepared various CaVO@C samples by changing the initial addition amount of $CaCl_2$ and glucose before calcination (Fig. S13, details can be found in the experimental section). Assuming that the concentration of Ca dopant mainly affects the rate performance and the thickness of the coated carbon layer may effectively influence the long-term cycling performance, we have conducted rate and cycling performance evaluation on the CaVO@C samples with various Ca dopant and coated carbon content, respectively (Fig. S14). It can be seen that the Ca doping amount and carbon content significantly influence the electrochemical performance of the samples. Based on our experiments, the amount of doped calcium and carbon have been optimized. We have chosen the sample with 50 % calcium content and 50 % carbon content as the optimal sample.

After optimization, the rate capability of the best-performed $Ca_{0.17}V_2O_{3\text{-}x}$@C material was evaluated. The inset in Fig. 2d shows the galvanostatic charge/discharge (GCD) curves at investigated current densities of 0.2 to 40 A g^{-1}. The GCD curves behave two obvious voltage plateaus, indicating the multiple-step reaction mechanism of Zn^{2+} and H^+ co-insertion/extraction process [36]. In Fig. 2d, reversible capacities of 426, 403, 390, 374, 353, 333, 316, 294, and 233 mAh g^{-1} can be obtained at current densities of 0.2, 0.5, 1, 2, 5, 10, 15, 20, and 40 A g^{-1}, respectively. When the rate is restored to 0.2 A g^{-1}, the electrode recovers an average capacity of 420 mAh g^{-1}, indicating the high reversibility of the cathode. The excellent rate performance demonstrates the ultra-fast Zn^{2+} storage ability for the $Ca_{0.17}V_2O_{3\text{-}x}$@C cathode. We then compared the electrochemical Zn^{2+} storage performance of our $Ca_{0.17}V_2O_{3\text{-}x}$@C cathode material with recently reported state-of-the-art AZIB cathode materials (Fig. 2e and Table S5) [8,36,42–52]. It is worth noting that the capacity, stability, and especially the rate performance of our $Ca_{0.17}V_2O_{3\text{-}x}$@C cathode material show great advantages at all current densities. Additionally, we have calculated the energy and power densities of the prepared $Ca_{0.17}V_2O_{3\text{-}x}$@C cathode material for comparison (Fig. 2f, details can be found in the experimental section). The Ragone plots in Fig. 2f show that the $Ca_{0.17}V_2O_{3\text{-}x}$@C has an exceptionally high energy density of 327 W h kg^{-1} and exhibits superior specific energies over a wide range of specific power densities, outperforming other reported representative cathode materials for AZIBs [32,53–63], suggesting its promising potential for future practical applications.

We further performed stability tests at various current densities ranging from 0.5 to 20 A^{-1} (Figs. 2g and S15). As shown in Fig. 2g, at a moderate rate of 5 A g^{-1}, the $Ca_{0.17}V_2O_{3\text{-}x}$@C cathode materials show excellent cycling stability with 94 % capacity retention (335 mAh g^{-1}) after 2000 cycles and almost 100 % Coulombic efficiency. On the contrary, the $V_2O_{3\text{-}x}$@C cathode only has 76 % capacity retention (142 mAh g^{-1}) after 1000 cycles. Even at a high current density of 20 A g^{-1}, the $Ca_{0.17}V_2O_{3\text{-}x}$@C cathode still shows a satisfied capacity retention of 82 % after 10,000 cycles (Fig. 2i). At a low current density of 0.5 A g^{-1} and relatively high current density of 10 A g^{-1}, the $Ca_{0.17}V_2O_{3\text{-}x}$@C cathode also exhibits much higher cycling stability performance over the undoped $V_2O_{3\text{-}y}$@C sample. The outstanding cycling performance of $Ca_{0.17}V_2O_{3\text{-}x}$@C cathode far exceeds those of many reported representative AZIB cathode materials (Fig. 2h and j) [36,64–69,71–76]. The above results demonstrate that the initial Ca-doped sample of $Ca_{0.17}V_2O_{3\text{-}x}$@C possesses high electrochemical reactivity, electron/ion mobility, and structure stability for sustainable aqueous Zn^{2+} storage.

The contribution of pseudocapacitance-like capacity to whole redox was then analyzed to evaluate the electrochemical reaction kinetics of the $Ca_{0.17}V_2O_{3\text{-}x}$@C cathode material for AZIBs (Fig. 3, details can be found in the experimental section in Supplementary Information). Fig. 3a shows the CV curves at various sweep rates. As the scanning speed increases from 0.1 to 1 mV s^{-1}, the curves keep similar shapes with little peak offsets, revealing the excellent electrochemical reaction reversibility. According to the log(*i*)-log (*v*) plots (Fig. 3b), the *b* values (a parameter for electrochemical kinetics evaluation) of the four redox peaks (denoted as peaks 1 to 4) are calculated to be 0.93, 0.90, 0.92, and 1.00, respectively. This suggests that the four electrochemical redox reactions involved in the charge/discharge process have excellent reaction dynamics. The contribution ratios of pseudocapacitance-like capacity at investigated sweep rates are calculated to be 91 % to 99 % for investigated sweep rates of 0.1–1 mV s^{-1} (Fig. 3c, d). Pseudocapacitive behavior indicates a rapid Faradaic process, including surface or near-surface redox reactions and rapid ion insertion/extration. The high surface reactivity of the V_2O_5-type carbon-coated materials generated through *in-situ* electrochemical conversion provides a high-density of reactive sites for surface charge storage and facilitates the penetration of the electrolyte into its interior, significantly improving the accessibility of internal active sites and effectively reducing the overall reaction energy barrier [80]. This capacititance effect is the main reason for the high-rate performance of the $Ca_{0.17}V_2O_{3\text{-}x}$@C cathode electrode.

To study the migration kinetics of Zn^{2+} during the charge and discharge process (Fig. 3e), galvanostatic intermittent titration technique (GITT) characterization was adopted to calculate the Zn^{2+} diffusion coefficient. The calculated D_{Zn} of $Ca_{0.17}V_2O_{3\text{-}x}$@C is in the range of 10^{-13} to 10^{-10} cm^2 s^{-1}, which is about 10 times that of $V_2O_{3\text{-}y}$@C (Fig. S16), and is 10^2 to 10^3 times higher than that of the Li^+ diffusion rate in $LiFePO_4$ and $LiCoO_2$ [87–89]. In comparison, the Zn^{2+} diffusion coefficient in $Ca_{0.17}V_2O_{3\text{-}x}$@C far exceeds those of many reported AZIB cathode materials [8,12,81–86]. The enhanced electrochemical reaction kinetics proved by the pseudocapacitance-like capacity contribution and Zn^{2+} diffusion coefficient analysis results can be attributed to the introduction of more oxygen vacancies originating from the initial Ca-doping that provides more active sites for Zn^{2+} storage and reduces electrostatic repulsion between Zn^{2+} and the host $Ca_{0.17}V_2O_{3\text{-}x}$@C material.

To understand the origin of the ultra-high rate Zn^{2+} storage performance for the synthesized $Ca_{0.17}V_2O_{3\text{-}x}$@C material, we have conducted experimental investigations and theoretical calculations (Fig. 4). Electrochemical impedance spectrum (EIS) results can offer a deep insight into mass transfer dynamics for electrochemical reactions. In Fig. 4a, after electrochemical cycling and stabilization, the $Ca_{0.17}V_2O_{3\text{-}x}$@C sample shows a distinct lower series mass transfer resistance (R_s), charge transfer resistance (R_{ct}), and ion transfer resistance (R_{ion}) than the undoped $V_2O_{3\text{-}y}$@C sample. The detailed fitted results and comparisons of R_s, R_{ct}, and R_{ion} based on the equivalent circuit are shown in Table S4. The linear section in the intermediate frequency range in the EIS spectrum (Warburg region) demonstrates the Warburg impedance. Thus, we further analyzed the Warburg region by plotting Z' as a function of $\omega^{-1/2}$

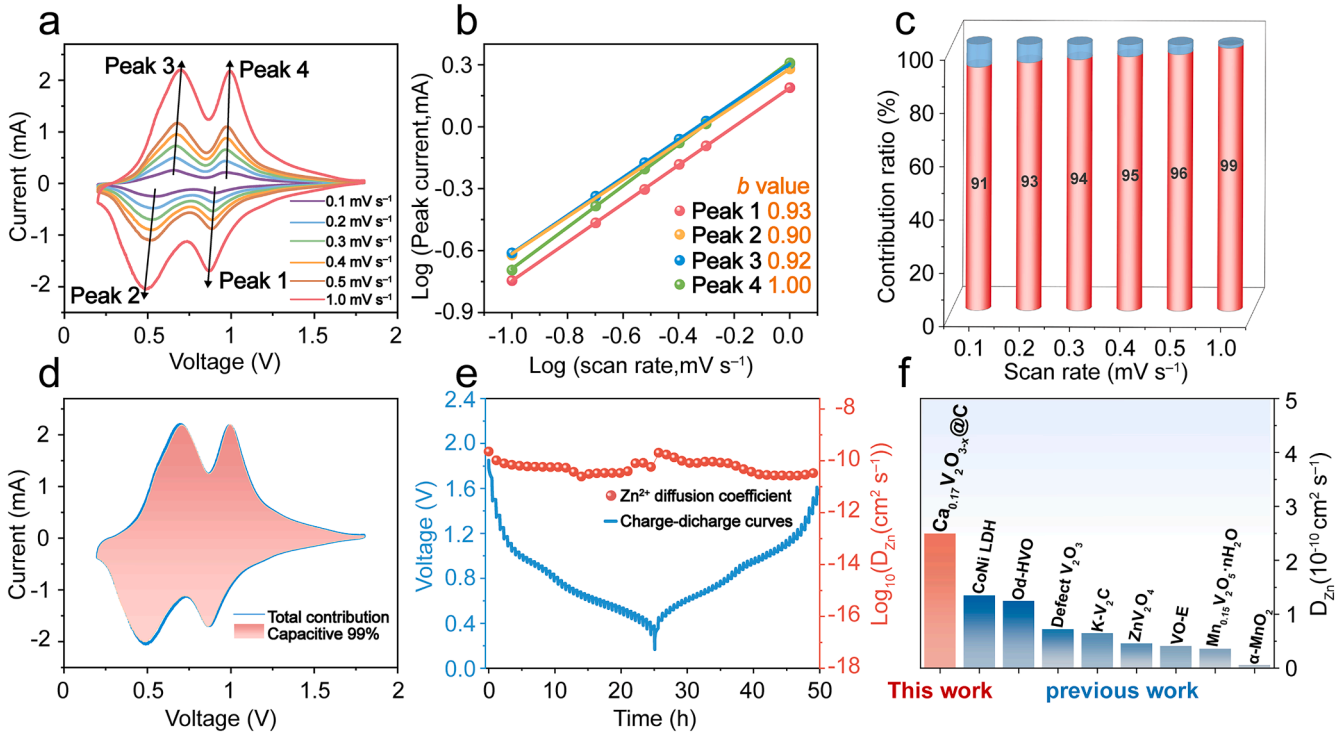

Fig. 3. Analysis on electrochemical reaction kinetics. (a) CV curves of $Ca_{0.17}V_2O_{3-x}$@C at scan rates of 0.1–1 mV s^{-1}. (b) The corresponding log (*i*, peak current) vs. Log (*v*, scan rate) plots at specific peak currents. (c) Contribution ratio of capacitive capacities and diffusion-controlled capacities at scan rates of 0.1–1.0 mV s^{-1}. (d) CV profile at 1 mV s^{-1} and the capacitive contribution (red region) to the total current. (e) Charge-discharge GITT curve of $Ca_{0.17}V_2O_{3-x}$@C at a current density of 0.1 A g^{-1} and the corresponding Zn^{2+} diffusion coefficient. (f) A comparison of the Zn^{2+} diffusion coefficients for the $Ca_{0.17}V_2O_{3-x}$@C sample in this work and some representative cathodes in previous work [8,12,81–86].

(Fig. 4b). The D_{Zn} can also be calculated from the slopes of the fitting lines (details are shown in the experimental section in Supporting information). The $Ca_{0.17}V_2O_{3-x}$@C electrode shows a higher D_{Zn} of 8.2 × 10^{-13} cm^2 s^{-1} than that of V_2O_{3-y}@C electrode (1.7 × 10^{-13} cm^2 s^{-1}), demonstrating that $Ca_{0.17}V_2O_{3-x}$@C is more favorable for electrochemical Zn^{2+} ion transportation. These EIS and Warburg region analysis results are consistent with the GITT results in Fig. 3e.

As discussed in previous work, the oxygen vacancy defects play an important role in the electrochemical Zn^{2+} storage energy density and rate performance [90,91], we further analyzed the evolution of oxygen vacancy defects after cycling and stabilization (Fig. 4c and d). In Fig. 4c, the oxygen vacancy defects in both doped and undoped samples are well restored. However, the oxygen vacancy defect ratio in $Ca_{0.17}V_2O_{3-x}$@C is much higher than that in V_2O_{3-y}@C, which is also supported by the EPR results shown in Fig. 4d. The EPR results of the $Ca_{0.17}V_2O_{3-x}$@C sample also show that the oxygen vacancy defects are highly stable during the electrochemical cycling process. The high stability of oxygen vacancy defects is responsible for the high-rate long-term performance (Figs. 2g, i and S15).

We further conducted DFT calculations to investigate the mechanism of the improved electrochemical Zn^{2+} storage performance for the initial Ca-doped sample. Because of the phase transition of V_2O_3 into layered V_2O_5-type cathode material after electrochemical stabilization in our findings, we select three model structures (i.e. perfect V_2O_5 (P-V_2O_5, oxygen vacancy free samples), oxygen vacancy defective V_2O_{5-x} (O_d-V_2O_{5-x}), and oxygen vacancy defective Ca doped V_2O_{5-x} (O_d-CaVO)) for calculation and comparison. We first evaluate the electrical properties of the investigated structures (Fig. 4e–j). As can be seen, after doping Ca, it produces a small impurity level that crosses the Fermi level (Fig. 4g), indicating the electrical conductivity of the Ca-doped material is highly improved. The introduced oxygen vacancy defects can narrow the band gap of V_2O_5 (from 2.13 eV for P-V_2O_5 to 2.03 eV for O_d-V_2O_{5-x}) and doping Ca can further enhance the electron mobility by reducing the band gap to 1.53 eV.

The charge distributions for the investigated three structures were drawn in Fig. 4k–m. The charge distribution is quite different for these structures. The more uneven the electron distribution, the more severe the polarization, resulting in more difficult Zn^{2+} ion adsorption/desorption. Results show that the uneven charge distribution can be regulated by introducing oxygen vacancy defects and further by Ca doping, which supports the improved electrochemical Zn^{2+} storage rate performance for the investigated $Ca_{0.17}V_2O_{3-x}$@C material. The charge distribution directly reflects the binding energies between Zn^{2+} and adsorption sites that the more severe the polarization, the higher the binding energy. Among the three investigated structures, O_d-CaVO shows the lowest binding energy of –0.24 eV (Table 1).

To reveal the possible Zn^{2+} migration pathway and transport energy barriers during the Zn^{2+} storage process, we have selected two optimized Zn^{2+} migration pathways after calculation (Figs. 4n–q and S17). Results show that Zn^{2+} transport properties can be greatly enhanced by introducing oxygen vacancy defects and further Ca doping. The O_d-CaVO structure, which combines oxygen vacancy defects and Ca doping possesses the lowest Zn^{2+} transport energy barrier of 0.39 eV compared with those of the other two structures (from 0.80 to 1.66 eV).

To explore the origin of the enhanced electrochemical stability of $Ca_{0.17}V_2O_{3-x}$@C for AZIBs, we then investigated the bond lengths of P-V_2O_5, O_d-V_2O_{5-x}, and O_d-CaVO structures before and after Zn^{2+} adsorption *via* theoretical calculations. The smaller the bond length, the higher the structural stability for electrochemical cycles. In Table 1 and Fig. S18, among the three structures, we can see that before Zn^{2+} adsorption, the O_d-CaVO structure shows the smallest V-O bond length of 1.75 Å. After Zn^{2+} adsorption, the O_d-CaVO structure shows the smallest V-O bond length of 1.76 Å and the largest Zn-O bond length of 2.84 Å. According to Lewis theory of acids and bases, O^{2-} ions can be regarded as a hard base and Ca^{2+} ions act as a hard acid, the binding of hard bases and hard acids can produce strong interaction forces, thus

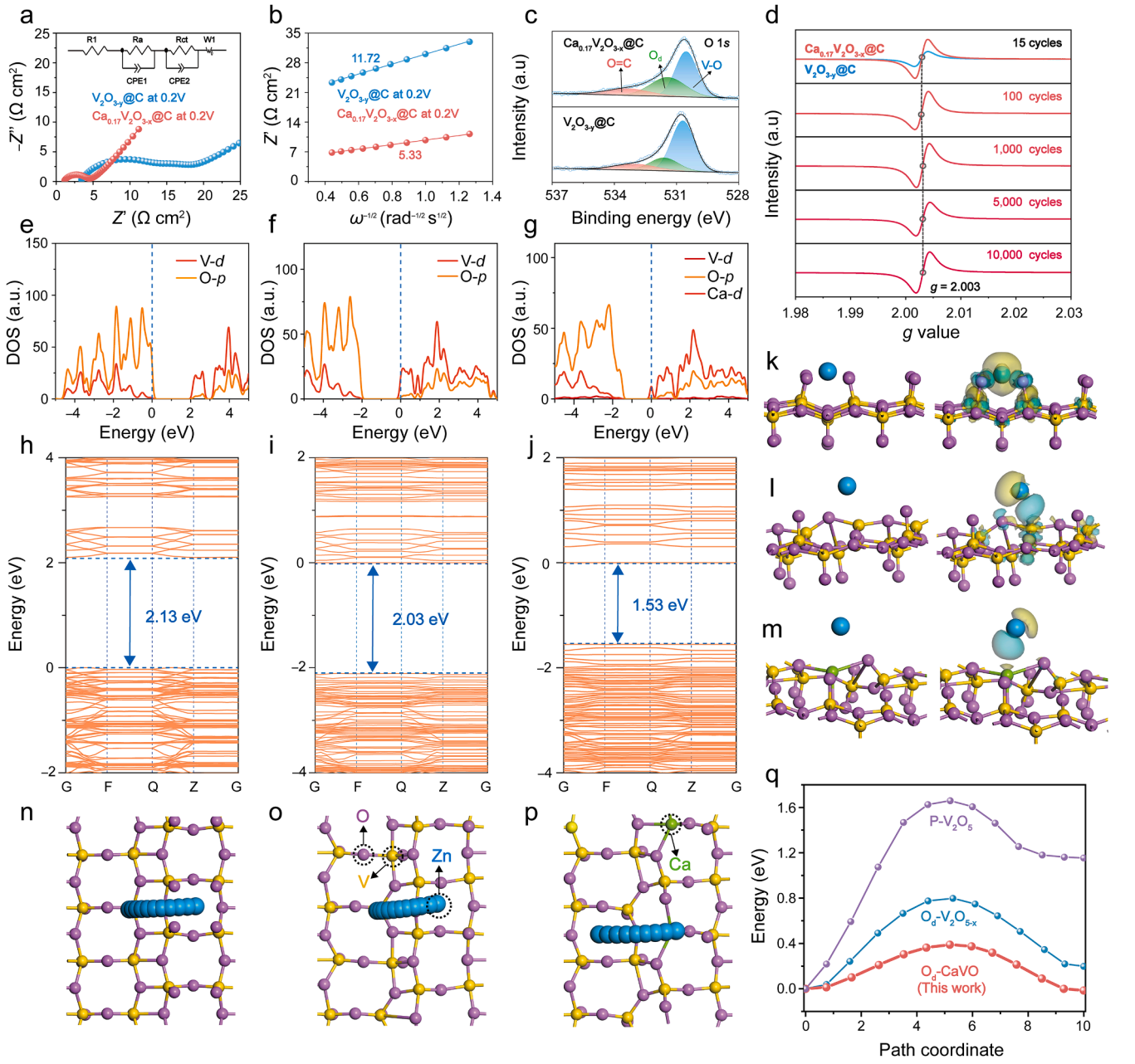

Fig. 4. Mechanistic study. (a) EIS spectra for $Ca_{0.17}V_2O_{3-x}$@C and V_2O_{3-y}@C cathodes after 15 cycles. The inset shows the equivalent circuit. (b) Plots of Z' vs. $\omega^{-1/2}$. (c) Deconvolution results of O 1*s* orbital of $Ca_{0.17}V_2O_{3-x}$@C and V_2O_{3-y}@C cathodes after 15 cycles. (d) EPR curves of $Ca_{0.17}V_2O_{3-x}$@C cathode after 15, 100, 1000, 5000, and 10,000 cycles and V_2O_{3-y}@C cathode after 15 cycles. Note that cathodes in (a–d) were disassembled from the coin cell batteries after cycling (cut-off at 0.2 V). (e–g) Calculated density of states and (h–j) band structures for perfect V_2O_5 (P-V_2O_5), oxygen vacancy defective V_2O_{5-x} (O_d-V_2O_{5-x}), and oxygen vacancy defective Ca doped V_2O_{5-x} (O_d-CaVO), respectively. (k–m) Structure geometry (side-view) and electron density difference of P-V_2O_5, O_d-V_2O_{5-x}, and O_d-CaVO samples after Zn^{2+} adsorption, respectively. Charge accumulation is in yellow and depletion is in blue. (n–p) Calculated possible migration pathways and (q) corresponding energy barriers for Zn^{2+} transport in P-V_2O_5, O_d-V_2O_{5-x}, and O_d-CaVO samples, respectively.

forming strong ionic bonds. The strong Ca-O and V-O bonds in the O_d-CaVO structure thus benefit the long-term Zn^{2+} storage stability. The largest Zn-O bond length in the O_d-CaVO structure indicates the favorable Zn^{2+} transportation characteristic. These results show that the O_d-CaVO structure is more stable and suitable for Zn^{2+} adsorption/desorption (or insertion/extraction) over the other two structures.

To verify the calculation results and get deep insight into the long-term stability of the developed $Ca_{0.17}V_2O_{3-x}$@C cathode for zinc ion storage, we further observed the separators after cycling by disassembling the coin cells and conducted elemental analysis using SEM-EDS characterization (Fig. S19). It can be seen that the separator's surface of the $Ca_{0.17}V_2O_{3-x}$@C electrode is smooth and clean after 2000 cycles 5 A g^{-1}, Fig. S19a–c). In sharp contrast, the separator's surface of the V_2O_{3-x}@C electrode shows severe dissolution of the cathode material after only 500 cycles (5 A g^{-1}, Fig. S19d). The detection of the V element on the separator's surface of the V_2O_{3-x}@C electrode from the EDS data indicates the significant dissolution of V (Fig. S19e and f). In brief, the initial doped strong Lewis acidic element of Ca in the cathode material plays a significant role in alleviating the dissolution of V and achieving long-term cycling stability (Fig. S19b and c). The observed inhibition effect on V element dissolution in the $Ca_{0.17}V_2O_{3-x}$@C electrode is ascribed to the increased bond strength of Ca-O and V-O. To investigate the ability of suppressing self-discharge of our system, we have observed the open-circuit voltage change of the assembled batteries resting for 36

Table 1
Investigation of the bond properties and Zn^{2+} adsorption energies for various structures *via* DFT calculations.

Structure	Status	V-O [Å]	Ca-O [Å]
P-V_2O_5	Before Zn^{2+} adsorption	1.85[a]	–
O_d-V_2O_{5-x}		1.90[a]	–
O_d-CaVO		1.75[a]	2.39[a]

Structure	Status	Zn-O [Å]	V-O [Å]	Ca-O [Å]	Adsorption energy [eV]
P-V_2O_5	After Zn^{2+} adsorption	2.02	1.84[a]	–	-2.25
O_d-V_2O_{5-x}		2.44	1.90[a]	–	-0.45
O_d-CaVO		2.84	1.76[a]	2.39[a]	-0.24

Note: a means an averaged length. The calculated structures and bond lengths are shown in Fig. S18.

h (Fig. S20a). It can be seen that the voltage of the Zn//$Ca_{0.17}V_2O_{3-x}$@C coin cell only decreased by 0.042 V after resting for 36 h, while the Zn//V_2O_{3-x}@C coin cell decreased by 0.167 V (Fig. S20b). Then, we investigated the self-discharge behaviors of the batteries after full-charged to simulate the practical using conditions (Fig. S20c). The $Ca_{0.17}V_2O_{3-x}$@C cathode retained 93 % of its initial capacity after 24 h of rest, significantly surpassing the 87 % retention observed for V_2O_{3-x} cathode after 15 h of rest (Fig. S20d). The high-capacity retention suggests that the Ca-doped cathode effectively suppresses side reactions and V dissolution [92]. Therefore, we conclude that a significant improvement in suppressing self-discharge behavior is achieved in our prepared $Ca_{0.17}V_2O_{3-x}$@C cathode.

Our experimental results and theoretical calculations demonstrate that the ultra-high rate and ultra-stable electrochemical Zn^{2+} storage energy performance of $Ca_{0.17}V_2O_{3-x}$@C originates from the high density of oxygen vacancy defects, enhanced electrical/ion conductivity, improved bonding strength induced by the initial Ca-doping and *in-situ* electrochemical activation process.

We were encouraged to explore the practical application potentials of the $Ca_{0.17}V_2O_{3-x}$@C material due to its impressive electrochemical performance in coin cell-type batteries. As shown in Fig. 5a, pouch cells were constructed using $Ca_{0.17}V_2O_{3-x}$@C as cathode, Zn foil as anode, and

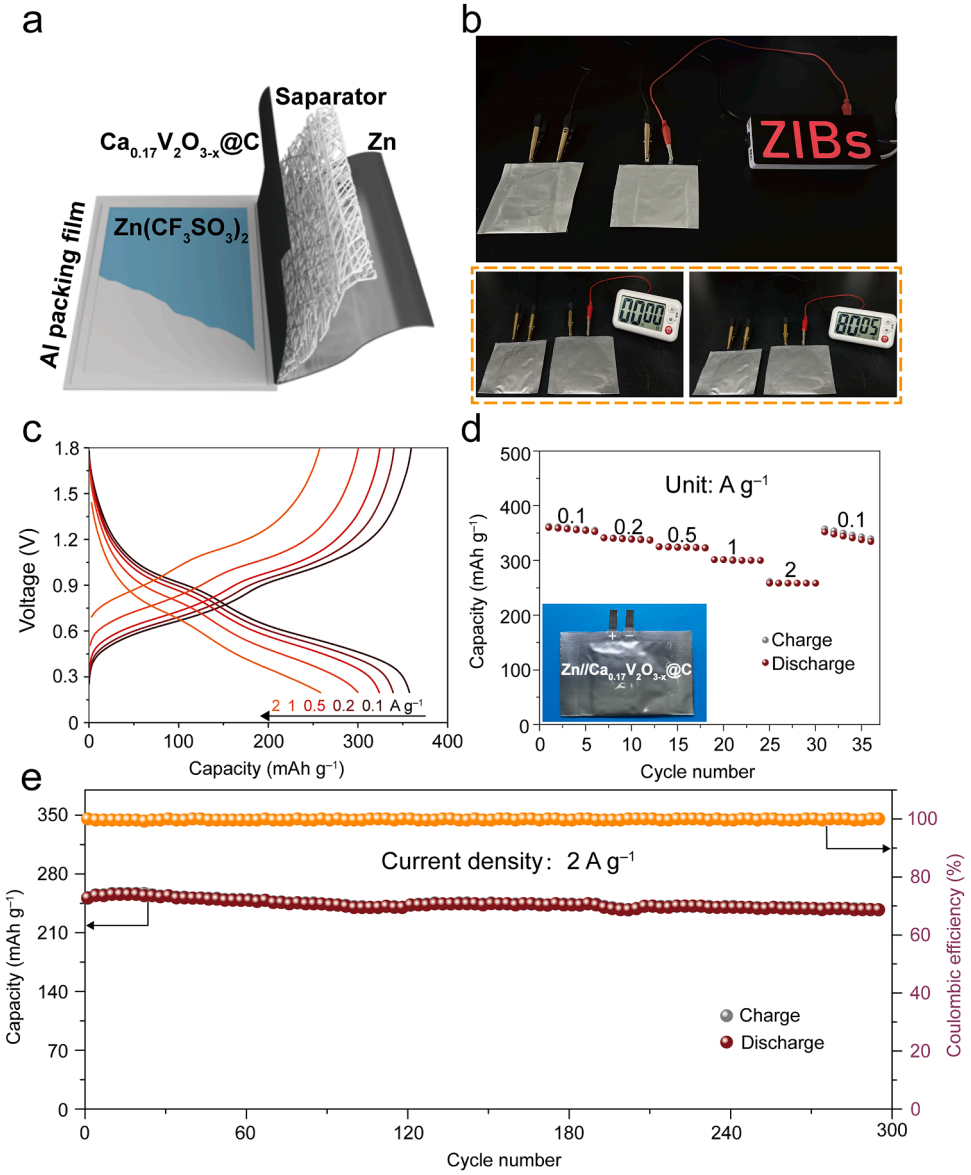

Fig. 5. Pouch cell performance. (a) A schematic of the structure of the fabricated Zn//$Ca_{0.17}V_2O_{3-x}$@C pouch cell. (b) Photographs of two series-connected pouch cells power an LED light and an electronic timer. (c) Rate capability and (d) GCD curves at various current densities. (e) Cycling performance and corresponding Coulombic efficiency of the pouch cell at 2 A g^{-1}.

then packed with Al-plastic film (details can be found in the experimental section). Two series-connected pouch cells can successfully light up an LED light and power an electronic timer for 80 min (Fig. 5b). The rate performance of the fabricated Zn//$Ca_{0.17}V_2O_{3-x}$@C pouch cell was evaluated. Fig. 5c shows the GCD curves at investigated current densities of 0.1 to 2 A g^{-1}, which are consistent with the GCD curves in coin cell batteries. In Fig. 5d, reversible cathode capacities of 357, 339, 324, 300, and 258 mAh g^{-1} can be obtained at current densities of 0.1, 0.2, 0.5, 1, and 2 A g^{-1}, respectively. When the rate is restored to 0.1 A g^{-1}, the electrode recovers to an average capacity of 341 mAh g^{-1}, confirming the highly reversible and high-rate characteristics of $Ca_{0.17}V_2O_{3-x}$@C for Zn^{2+} storage in practical pouch cells. Furthermore, the long-term cycling stability performance of the pouch cell was investigated at a moderate current density of 2 A g^{-1} (Fig. 5e). After 300 cycles, the capacity remains at 238 mAh g^{-1} with 95 % capacity retention and near 100 % Coulombic efficiency, indicating its excellent cycling stability. We have also investigated the swelling situation for the pouch cell before and after cycling. It can be observed that after 300 cycles at 2 A g^{-1} (Fig. S21), the pouch cell does not show significant swelling, indicating that no severe HER reaction has occurred in the system, from the CV curves of $Ca_{0.17}V_2O_{3-x}$@C for 15 cycles in Fig. 2a, there is no additional reduction peak appears at the low voltage of 0.2 V, indicating that no serious HER reaction has occurred in the system. Thus, we believe that no serious hydrogen evolution reaction was occurred in our system. The remarkable electrochemical performance of the pouch cells demonstrates the promising practical AZIB application potentials of the $Ca_{0.17}V_2O_{3-x}$@C material.

4. Conclusions

In summary, we have reported a simple and effective approach to achieve ultra-fast and ultra-stable aqueous Zn^{2+} storage performance for phase transformation typed AZIB cathode material of vanadium oxide (V_2O_3) *via* forming strong Lewis electron-pair bonding between doped Ca and lattice O in the crystal. The core role of the initial-doped Ca in this strategy generates abundant oxygen vacancy defects in the carbon-encapsulated vanadium oxide ($Ca_{0.17}V_2O_{3-x}$@C) and we find that the initial-doped Ca as well as the generated oxygen vacancy defects can be well restored after phase transition from activation and even long-term cycling. The strong Lewis acidic doping element of Ca improves the electrical conductivity and builds considerably strong bonding of Ca-O and V-O in the phase transition product of a layered V_2O_5-like structure. The oxygen vacancy defects in the phase transition product exhibit optimal Zn^{2+} binding energy and ultra-low Zn-ion transport barrier. Based on these results, we prove that the band and bond structures of the phase-transformed vanadium oxide are optimized by the initial-doped Ca and oxygen vacancy defects, thereby realizing enhanced electrochemical Zn^{2+} storage kinetics and stability in this work. The reported strategy of Lewis acidic elemental doping induced microstructure engineering (such as defects, electronic structure, and bonding) of vanadium oxide may be expanded to other kinds of phase-transformed compounds for efficient, highly stable, and ultra-fast energy storage applications.

CRediT authorship contribution statement

Siyuan Zhang: Writing – original draft, Validation, Formal analysis, Data curation. **Leiming Lang:** Writing – review & editing, Validation, Supervision, Resources, Formal analysis. **Yingjie Hu:** Validation, Methodology. **Jianhua Sun:** Formal analysis. **Guangxiang Liu:** Formal analysis. **Guoqiang Luo:** Formal analysis. **Linfeng Hu:** Writing – review & editing, Formal analysis. **Wenshu Chen:** Writing – review & editing, Validation, Supervision, Resources, Funding acquisition, Conceptualization.

Declaration of competing interest

The authors declare that they have no known competing financial interests or personal relationships that could have appeared to influence the work reported in this paper.

Data availability

Data will be made available on request.

Acknowledgments

This work was finically supported by the National Natural Science Foundation of China (Grant No's. 52101261, 52171203, and 52371214); the General Program of Natural Science Foundation of Jiangsu Province, China (Grant No. BK20221179); the China Postdoctoral Science Foundation (Grant No's. 2021M691513 and 2022T150307).

Supplementary materials

Supplementary material associated with this article can be found, in the online version, at doi:10.1016/j.ensm.2024.103801.

References

[1] Y. Liang, Y. Yao, Designing modern aqueous batteries, Nat. Rev. Mater. 8 (2023) 109–122, https://doi.org/10.1038/s41578-022-00511-3.
[2] S. Mallapaty, How China could be carbon neutral by mid-century, Nature 586 (2020) 482–483, https://doi.org/10.1038/d41586-020-02927-9.
[3] D. Jordan, T. Barnes, N. Haegel, I. Repins, Build solar-energy systems to last-save billions, Nature 600 (2021) 215–217, https://doi.org/10.1038/d41586-021-03626-9.
[4] W. Chen, J. Gu, Q. Liu, M. Yang, C. Zhan, X. Zang, T.A. Pham, G. Liu, W. Zhang, D. Zhang, Two-dimensional quantum-sheet films with sub-1.2 nm channels for ultrahigh-rate electrochemical capacitance, Nat. Nanotechnol. 17 (2022) 153–158, https://doi.org/10.1038/s41565-021-01020-0.
[5] Q. Wang, W. Zhou, Y. Zhang, H. Jin, X. Li, T. Zhang, B. Wang, R. Zhao, J. Zhang, W. Li, Y. Qiao, C. Jia, D. Zhao, D. Chao, Rescue of dead MnO2 for stable electrolytic Zn-Mn redox-flow battery: a metric of mediated and catalytic kinetics, Natl. Sci. Rev. 11 (2024) nwae230, https://doi.org/10.1093/nsr/nwae230.
[6] B. Wang, W. Zhou, Y. Zhang, T. Zhang, X. Li, Y. Feng, R. Zhao, W. Li, A. Elzatahry, Y. Hassan, D. Zhao, D. Chao, An energetic K+-S aqueous battery with 96% sulfur redox utilization, Joule 8 (2024) 1–16, https://doi.org/10.1016/j.joule.2024.03.021.
[7] Z. Sun, F. Bu, Y. Zhang, W. Zhou, X. Li, X. Liu, H. Jin, S. Ding, T. Zhang, L. Wang, H. Li, W. Li, C. Zhang, D. Zhao, Y. Wang, D. Chao, Electron-donating conjugation effect modulated Zn^{2+} reduction reaction for separator-free aqueous zinc batteries, Angew. Chem. Int. Ed. 63 (2024) e202402987, https://doi.org/10.1002/anie.202402987.
[8] J. Ding, H. Zheng, H. Gao, Q. Liu, Z. Hu, L. Han, S. Wang, S. Wu, S. Fang, S. Chou, *In situ* lattice tunnel distortion of vanadium trioxide for enhancing zinc ion storage, Adv. Energy Mater. 11 (2021) 2100973, https://doi.org/10.1002/aenm.202100973.
[9] K. Zhu, S. Wei, H. Shou, F. Shen, S. Chen, P. Zhang, C. Wang, Y. Cao, X. Guo, M. Luo, Defect engineering on V_2O_3 cathode for long-cycling aqueous zinc metal batteries, Nat. Commun. 12 (2021) 6878, https://doi.org/10.1038/s41467-021-27203-w.
[10] Y. Lu, T. Zhu, W. van den Bergh, M. Stefik, K. Huang, A high performing Zn-ion battery cathode enabled by *in situ* transformation of V2O5 atomic layers, Angew. Chem. Int. Ed. 132 (2020) 17152–17159, https://doi.org/10.1002/ange.202006171.
[11] L. Wang, K.W. Huang, J. Chen, J. Zheng, Ultralong cycle stability of aqueous zinc-ion batteries with zinc vanadium oxide cathodes, Sci. Adv. 5 (2019) eaax4279, https://doi.org/10.1126/sciadv.aax4279.
[12] H. Geng, M. Cheng, B. Wang, Y. Yang, Y. Zhang, C.C. Li, Electronic structure regulation of layered vanadium oxide via interlayer doping strategy toward superior high-rate and low-temperature zinc-ion batteries, Adv. Funct. Mater. 30 (2020) 1907684, https://doi.org/10.1002/adfm.201907684.
[13] L. Ma, N. Li, C. Long, B. Dong, D. Fang, Z. Liu, Y. Zhao, X. Li, J. Fan, S. Chen, Achieving both high voltage and high capacity in aqueous zinc-ion battery for record high energy density, Adv. Funct. Mater. 29 (2019) 1906142, https://doi.org/10.1002/adfm.201906142.
[14] B.T. Liu, X.M. Shi, X.Y. Lang, L. Gu, Z. Wen, M. Zhao, Q. Jiang, Extraordinary pseudocapacitive energy storage triggered by phase transformation in hierarchical vanadium oxides, Nat. Commun. 9 (2018) 1375, https://doi.org/10.1038/s41467-018-03700-3.

[15] J. Zheng, C. Zhan, K. Zhang, W. Fu, Q. Nie, M. Zhang, Z. Shen, Rapid electrochemical activation of V_2O_3@ C cathode for high-performance zinc-ion batteries in water-in-salt electrolyte, ChemSusChem 15 (2022) e202200075, https://doi.org/10.1002/cssc.202200075.

[16] X. Chen, Q. Kong, X. Wu, X. An, J. Zhang, Q. Wang, W. Yao, V_2O_3@C optimized by carbon regulation strategy for ultra long-life aqueous zinc-ion batteries, Chem. Eng. J. 451 (2023) 138765, https://doi.org/10.1016/j.cej.2022.138765.

[17] Y. Duan, Z. Geng, D. Zhang, Q. Wang, *In situ* electrochemically activated V_2O_3@ MXene cathode for a super high-rate and long-life Zn-ion battery, Dalton Trans. 53 (2024) 7023–7034, https://doi.org/10.1039/d4dt00488d.

[18] W. Wang, V.S. Kale, Z. Cao, Y. Lei, S. Kandambeth, G. Zou, Y. Zhu, E. Abouhamad, O. Shekhah, L. Cavallo, M. Eddaoudi, H.N. Alshareef, Molecular engineering of covalent organic framework cathodes for enhanced zinc-ion batteries, Adv. Mater. 33 (2021) 2103617, https://doi.org/10.1002/adma.202103617.

[19] Y. Ding, Y. Peng, S. Chen, X. Zhang, Z. Li, L. Zhu, L.E. Mo, L. Hu, Hierarchical porous metallic V_2O_3@ C for advanced aqueous zinc-ion batteries, ACS Appl. Mater. Interfaces 11 (2019) 44109–44117, https://doi.org/10.1021/acsami.9b13729.

[20] S. Yang, Y. Zhang, Y. Zhang, J. Deng, N. Chen, S. Xie, Y. Ma, Z. Wang, Designing anti-swelling nanocellulose separators with stable and fast ion transport channels for efficient aqueous zinc-ion batteries, Adv. Funct. Mater. 33 (2023) 2304280, https://doi.org/10.1002/adfm.202304280.

[21] J.S. Park, S. Yang, Y.C. Kang, Boosting the electrochemical performance of V_2O_3 by anchoring on carbon nanotube microspheres with macrovoids for ultrafast and long-life aqueous zinc-ion batteries, Small Methods 5 (2021) 2100578, https://doi.org/10.1002/smtd.202100578.

[22] Y. Li, H. Liu, M. Ma, W. Peng, Y. Li, X. Fan, N-Doping-induced amorphization for achieving ultrastable aqueous zinc-ion batteries, ACS Appl. Mater. 16 (2024) 26079–26087, https://doi.org/10.1021/acsami.4c01360.

[23] S.J. Clark, M.D. Segall, C.J. Pickard, P.J. Hasnip, M.J. Probert, K. Refson, M. C. Payne, First principles methods using CASTEP, Z. Kristallogr. Cryst. Mater. 220 (2005) 567–570, https://doi.org/10.1524/zkri.220.5.567.65075.

[24] J.P. Perdew, K. Burke, M. Ernzerhof, Generalized gradient approximation made simple, Phys. Rev. Lett. 77 (1996) 3865, https://doi.org/10.1103/PhysRevLett.77.3865.

[25] N. Govind, M. Petersen, G. Fitzgerald, D. King-Smith, J. Andzelm, A generalized synchronous transit method for transition state location, Comput. Mater. Sci. 28 (2003) 250–258, https://doi.org/10.1016/s0927-0256(03)00111-3.

[26] M. Bao, Z. Zhang, X. An, J. Liu, J. Feng, B. Xi, S. Xiong, Introducing Ce ions and oxygen defects into V_2O_5 nanoribbons for efficient aqueous zinc ion storage, Nano Res. 16 (2023) 2445–2453, https://doi.org/10.1007/s12274-022-4990-2.

[27] W. Yang, L. Dong, W. Yang, C. Xu, G. Shao, G. Wang, 3D oxygen-defective potassium vanadate/carbon nanoribbon networks as high-performance cathodes for aqueous zinc-ion batteries, Small Methods 4 (2020) 1900670, https://doi.org/10.1002/smtd.201900670.

[28] X. Liang, L. Yan, W. Li, Y. Bai, C. Zhu, Y. Qiang, B. Xiong, B. Xiang, X. Zou, Flexible high-energy and stable rechargeable vanadium-zinc battery based on oxygen defect modulated V_2O_5 cathode, Nano Energy 87 (2021) 106164, https://doi.org/10.1016/j.nanoen.2021.106164.

[29] H. Luo, B. Wang, F. Wang, J. Yang, F. Wu, Y. Ning, Y. Zhou, D. Wang, H. Liu, S. Dou, Anodic oxidation strategy toward structure-optimized V_2O_3 cathode via electrolyte regulation for Zn-ion storage, ACS Nano 14 (2020) 7328–7337, https://doi.org/10.1021/acsnano.0c02658.

[30] J. Hong, L. Xie, C. Shi, X. Lu, X. Shi, J. Cai, Y. Wu, L. Shao, Z. Sun, High-performance aqueous zinc-ion batteries based on multidimensional V_2O_3 nanosheets@single-walled carbon nanohorns@reduced graphene oxide composite and optimized electrolyte, Small Methods 8 (6) (2024) 2300205, https://doi.org/10.1002/smtd.202300205.

[31] X. Wang, Z. Zhang, M. Huang, J. Feng, S. Xiong, B. Xi, *In situ* electrochemically activated vanadium oxide cathode for advanced aqueous Zn-ion batteries, Nano Lett. 22 (2022) 119–127, https://doi.org/10.1021/acs.nanolett.1c03409.

[32] D. Kundu, B.D. Adams, V. Duffort, S.H. Vajargah, L.F. Nazar, A high-capacity and long-life aqueous rechargeable zinc battery using a metal oxide intercalation cathode, Nat. Energy 1 (2016) 16119, https://doi.org/10.1038/nenergy.2016.119.

[33] K. Zhu, T. Wu, W. van den Bergh, M. Stefik, K. Huang, $Zn_{0.52}V_2O_{5\text{-}a}$·1.8 H_2O cathode stabilized by *in situ* phase transformation for aqueous zinc-ion batteries with ultra-long cyclability, Acs Nano 15 (2021) 10678–10688, https://doi.org/10.1021/acsnano.1c03684.

[34] X. Wang, Z. Zhang, S. Xiong, F. Tian, Z. Feng, Y. Jia, J. Feng, B. Xi, A high-rate and ultrastable aqueous zinc-ion battery with a novel MgV_2O_6·1.7H_2O nanobelt cathode, Small 17 (2021) 2100318, https://doi.org/10.1002/smll.202100318.

[35] C. Liu, Z. Neale, J. Zheng, X. Jia, J. Huang, M. Yan, M. Tian, M. Wang, J. Yang, G. Cao, Expanded hydrated vanadate for high-performance aqueous zinc-ion batteries, Energy Environ. Sci. 12 (2019) 2273–2285, https://doi.org/10.1039/c9ee00956f.

[36] W. Liang, D. Rao, T. Chen, R. Tang, J. Li, H. Jin, $Zn_{0.52}V_2O_{5\text{-}a}$·1.8 H_2O cathode stabilized by *in situ* phase transformation for aqueous zinc-ion batteries with ultra-long cyclability, Angew. Chem. Int. Ed. 61 (2022) e202207779, https://doi.org/10.1002/anie.202207779.

[37] H. Wang, F. Liu, R. Yu, J. Wu, Unraveling the reaction mechanisms of electrode materials for sodium-ion and potassium-ion batteries by *in situ* transmission electron microscopy, Int. Mater. 1 (2022) 196–212, https://doi.org/10.1002/idm2.12008.

[38] Y. Huang, The discovery of cathode materials for lithium-ion batteries from the view of interdisciplinarity, Int. Mater. 1 (2022) 323–329, https://doi.org/10.1002/idm2.12048.

[39] L. Wang, B. Zhang, W. Zhou, Z. Zhao, X. Liu, R. Zhao, Z. Sun, H. Li, X. Wang, T. Zhang, H. Jin, W. Li, A. Elzatahry, Y. Hassan, H.J. Fan, D. Zhao, D. Chao, Tandem chemistry with Janus mesopores accelerator for efficient aqueous batteries, J. Am. Chem. Soc. 146 (2024) 6199–6208, https://doi.org/10.1021/jacs.3c14019.

[40] T. Lv, G. Zhu, S. Dong, Q. Kong, Y. Peng, S. Jiang, G. Zhang, Z. Yang, S. Yang, X. Dong, H. Pang, Y. Zhang, Co-intercalation of dual charge carriers in metal-ion-confining layered vanadium oxide nanobelts for aqueous zinc-ion batteries, Angew. Chem. Int. Ed. 62 (2023) e202216089, https://doi.org/10.1002/anie.202216089.

[41] I.R. Tay, J. Xue, W.S.V. Lee, Methods for characterizing intercalation in aqueous zinc ion battery cathodes: a review, Adv. Sci. 10 (2023) 2198–3844, https://doi.org/10.1002/advs.202303211.

[42] J. Kim, S.H. Lee, C. Park, H.S. Kim, J.H. Park, K.Y. Chung, H. Ahn, Controlling vanadate nanofiber interlayer via intercalation with conducting polymers: cathode material design for rechargeable aqueous zinc ion batteries, Adv. Funct. Mater. 31 (2021) 2100005, https://doi.org/10.1002/adfm.202100005.

[43] X. Zhu, Z. Cao, W. Wang, H. Li, J. Dong, S. Gao, D. Xu, L. Li, J. Shen, M. Ye, Superior-performance aqueous zinc-ion batteries based on the *in situ* growth of MnO_2 nanosheets on V2CTX MXene, ACS Nano 15 (2021) 2971–2983, https://doi.org/10.1021/acsnano.0c09205.

[44] J. Meng, Y. Song, Z. Qin, Z. Wang, X. Mu, J. Wang, X.X. Liu, Cobalt-nickel double hydroxide toward mild aqueous zinc-ion batteries, Adv. Funct. Mater. 32 (2022) 2204026, https://doi.org/10.1002/adfm.202204026.

[45] Y. Zhao, S. Liang, X. Shi, Y. Yang, Y. Tang, B. Lu, J. Zhou, Synergetic effect of alkali-site substitution and oxygen vacancy boosting vanadate cathode for super-stable potassium and zinc storage, Adv. Funct. Mater. 32 (2022) 2203819, https://doi.org/10.1002/adfm.202203819.

[46] D.S. Liu, Y. Zhang, S. Liu, L. Wei, S. You, D. Chen, M. Ye, Y. Yang, X. Rui, Y. Qin, C. C. Li, Regulating the electrolyte solvation structure enables ultralong lifespan vanadium-based cathodes with excellent low-temperature performance, Adv. Funct. Mater. 32 (2022) 2111714, https://doi.org/10.1002/adfm.202111714.

[47] W. Shi, B. Yin, Y. Yang, M.B. Sullivan, J. Wang, Y.W. Zhang, Z.G. Yu, W.S.V. Lee, J. Xue, Unravelling V_6O_{13} diffusion pathways via CO_2 modification for high-performance zinc ion battery cathode, ACS Nano 15 (2021) 1273–1281, https://doi.org/10.1021/acsnano.0c08432.

[48] X. Wang, Y. Li, S. Wang, F. Zhou, P. Das, C. Sun, S. Zheng, Z.S. Wu, 2D amorphous V_2O_5/graphene heterostructures for high-safety aqueous Zn-ion batteries with unprecedented capacity and ultrahigh rate capability, Adv. Energy Mater. 10 (2020) 2000081, https://doi.org/10.1002/aenm.202000081.

[49] S. Liu, H. Zhu, B. Zhang, G. Li, H. Zhu, Y. Ren, H. Geng, Y. Yang, Q. Liu, C.C. Li, Tuning the kinetics of zinc-ion insertion/extraction in V_2O_5 by *in situ* polyaniline intercalation enables improved aqueous zinc-ion storage performance, Adv. Mater. 32 (2020) 2001113, https://doi.org/10.1002/adma.202001113.

[50] D. Chao, C. Zhu, M. Song, P. Liang, X. Zhang, T. Nguyen Huy, H. Zhao, J. Wang, R. Wang, H. Zhang, H.J. Fan, A high-rate and stable quasi-solid-state zinc-ion battery with novel 2D layered zinc orthovanadate array, Adv. Mater. 30 (2018) 1803181, https://doi.org/10.1002/adma.201803181.

[51] X. Li, M. Li, Q. Yang, H. Li, H. Xu, Z. Chai, K. Chen, Z. Liu, Z. Tang, L. Ma, Z. Huang, B. Dong, X. Yin, Q. Huang, C. Zhi, Phase transition induced unusual electrochemical performance of V2CTX MXene for aqueous zinc hybrid-ion battery, ACS Nano 14 (2020) 541–551, https://doi.org/10.1021/acsnano.9b06866.

[52] L. Wang, M. Peng, J. Chen, X. Tang, L. Li, T. Hu, K. Yuan, Y. Chen, High energy and power zinc ion capacitors: a dual-ion adsorption and reversible chemical adsorption coupling mechanism, ACS Nano 16 (2022) 2877–2888, https://doi.org/10.1021/acsnano.1c09936.

[53] M.H. Alfaruqi, J. Gim, S. Kim, J. Song, P. Duong Tung, J. Jo, Z. Xiu, V. Mathew, J. Kim, A layered δ-MnO_2 nanoflake cathode with high zinc-storage capacities for eco-friendly battery applications, Electrochem. Commun. 60 (2015) 121–125, https://doi.org/10.1016/j.elecom.2015.08.019.

[54] P. He, M. Yan, G. Zhang, R. Sun, L. Chen, Q. An, L. Mai, Layered VS_2 nanosheet-based aqueous Zn ion battery cathode, Adv. Energy Mater. 7 (2017) 1601920, https://doi.org/10.1002/aenm.201601920.

[55] G. Li, Z. Yang, Y. Jiang, C. Jin, W. Huang, X. Ding, Y. Huang, Towards polyvalent ion batteries: a zinc-ion battery based on NASICON structured $Na_3V_2(PO_4)_3$, Nano Energy 25 (2016) 211–217, https://doi.org/10.1016/j.nanoen.2016.04.051.

[56] X. Wang, Y. Liu, Z. Wei, J. Hong, H. Liang, M. Song, Y. Zhou, X. Huang, MXene-boosted imine cathodes with extended conjugated structure for aqueous zinc-ion batteries, Adv. Mater. 34 (2022) 2206812, https://doi.org/10.1002/adma.202206812.

[57] C. Xia, J. Guo, Y. Lei, H. Liang, C. Zhao, H.N. Alshareef, Rechargeable aqueous zinc-ion battery based on porous framework zinc pyrovanadate intercalation cathode, Adv. Mater. 30 (2018) 1705580, https://doi.org/10.1002/adma.201705580.

[58] C. Xia, J. Guo, P. Li, X. Zhang, H.N. Alshareef, Highly stable aqueous zinc-ion storage using a layered calcium vanadium oxide bronze cathode, Angew. Chem. Int. Ed. 57 (2018) 3943–3948, https://doi.org/10.1002/anie.201713291.

[59] C. Xu, B. Li, H. Du, F. Kang, Energetic zinc ion chemistry: the rechargeable zinc ion battery, Angew. Chem. Int. Ed. 51 (2012) 933–935, https://doi.org/10.1002/anie.201106307.

[60] M. Yan, P. He, Y. Chen, S. Wang, Q. Wei, K. Zhao, X. Xu, Q. An, Y. Shuang, Y. Shao, K.T. Mueller, L. Mai, J. Liu, J. Yang, Water-lubricated intercalation in V_2O_5·nH_2O for high-capacity and high-rate aqueous rechargeable zinc batteries, Adv. Mater. 30 (2018) 1703725, https://doi.org/10.1002/adma.201703725.

[61] L. Zhang, L. Chen, X. Zhou, Z. Liu, Towards high-voltage aqueous metal-ion batteries beyond 1.5 V: the Zinc/Zinc hexacyanoferrate system, Adv. Energy Mater. 5 (2015) 1400930, https://doi.org/10.1002/aenm.201400930.

[62] N. Zhang, F. Cheng, J. Liu, L. Wang, X. Long, X. Liu, F. Li, J. Chen, Rechargeable aqueous zinc-manganese dioxide batteries with high energy and power densities, Nat. Commun. 8 (2017) 450, https://doi.org/10.1038/s41467-017-00467-x.
[63] N. Zhang, F. Cheng, Y. Liu, Q. Zhao, K. Lei, C. Chen, X. Liu, J. Chen, Cation-deficient spinel $ZnMn_2O_4$ cathode in Zn $(CF_3SO_3)_2$ electrolyte for rechargeable aqueous Zn-ion battery, J. Am. Chem. Soc. 138 (2016) 12894–12901, https://doi.org/10.1021/jacs.6b05958.
[64] K. Zhu, T. Wu, K. Huang, A high capacity bilayer cathode for aqueous Zn-ion batteries, ACS Nano 13 (2019) 14447–14458, https://doi.org/10.1021/acsnano.9b08039.
[65] S. Chen, K. Li, K.S. Hui, J. Zhang, Regulation of lamellar structure of vanadium oxide via polyaniline intercalation for high-performance aqueous zinc-ion battery, Adv. Funct. Mater. 30 (2020) 2003890, https://doi.org/10.1002/adfm.202003890.
[66] K. Zhu, T. Wu, S. Sun, W. van den Bergh, M. Stefik, K. Huang, Synergistic H^+/Zn^{2+} dual ion insertion mechanism in high-capacity and ultra-stable hydrated VO_2 cathode for aqueous Zn-ion batteries, Energy Storage Mater. 29 (2020) 60–70, https://doi.org/10.1016/j.ensm.2020.03.030.
[67] S. Wei, S. Chen, X. Su, Z. Qi, C. Wang, B. Ganguli, P. Zhang, K. Zhu, Y. Cao, Q. He, D. Cao, X. Guo, W. Wen, X. Wu, P.M. Ajayan, L. Song, Manganese buffer induced high-performance disordered MnVO cathodes in zinc batteries, Energy Environ. Sci. 14 (2021) 3954–3964, https://doi.org/10.1039/d1ee00590a.
[68] Y. Zhao, Y. Huang, F. Wu, R. Chen, L. Li, High-performance aqueous zinc batteries based on organic/organic cathodes integrating multiredox centers, Adv. Mater. 33 (2021) 2106469, https://doi.org/10.1002/adma.202106469.
[69] L. Ding, L. Wang, J. Gao, T. Yan, H. Li, J. Mao, F. Song, S. Fedotov, L.Y. Chang, N. Li, Facile Zn^{2+} desolvation enabled by local coordination engineering for long-cycling aqueous zinc-ion batteries, Adv. Funct. Mater. 33 (2023) 2301648, https://doi.org/10.1002/adfm.202301648.
[70] C. Dong, J. Zhang, C. Huang, R. Liu, Z. Xia, S. Lu, L. Wang, L. Zhang, L. Chen, Anchored VN quantum dots boosting high capacity and cycle durability of $Na_3V_2(PO_4)_3$@NC cathode for aqueous zinc-ion battery and organic sodium-ion battery, Small (2024) 2402927, https://doi.org/10.1002/smll.202402927.
[71] D. Luo, H. He, L. Zeng, H. Yu, X. Li, C. Zhang, Steering *in-situ* low-voltage phase transition from spinel to layered cathode for high-performance zinc-ion batteries, Energy Storage Mater. 67 (2024) 103278, https://doi.org/10.1016/j.ensm.2024.103278.
[72] L. Dong, W. Yang, W. Yang, C. Wang, Y. Li, C. Xu, S. Wan, F. He, F. Kang, G. Wang, High-power and ultralong-life aqueous zinc-ion hybrid capacitors based on pseudocapacitive charge storage, Nanomicro Lett. 11 (2019) 1–9, https://doi.org/10.1007/s40820-019-0328-3.
[73] J. Yin, W. Zhang, W. Wang, N.A. Alhebshi, N. Salah, H.N. Alshareef, Electrochemical zinc ion capacitors enhanced by redox reactions of porous carbon cathodes, Adv. Energy Mater. 10 (2020) 2001705, https://doi.org/10.1002/aenm.202001705.
[74] W.G. Kidanu, J. Hur, H.W. Choi, M.I. Kim, I.T. Kim, High capacity and inexpensive multivalent cathode materials for aqueous rechargeable Zn-ion battery fabricated via *in situ* electrochemical oxidation of VO2 nanorods, J. Power Sources 523 (2022) 231060, https://doi.org/10.1016/j.jpowsour.2022.231060.
[75] Y. Qi, J. Huang, L. Yan, Y. Cao, J. Xu, D. Bin, M. Liao, Y. Xia, Towards high-performance aqueous zinc-ion battery via cesium ion intercalated vanadium oxide nanorods, Chem. Eng. J. 442 (2022) 136349, https://doi.org/10.1016/j.cej.2022.136349.
[76] J. Wang, Z. Liu, H.g. Wang, F. Cui, G. Zhu, Integrated pyrazine-based porous aromatic frameworks/carbon nanotube composite as cathode materials for aqueous zinc ion batteries, Chem. Eng. J. 450 (2022) 138051, https://doi.org/10.1016/j.cej.2022.138051.
[77] A. García-Sánchez, E. Alvarez-Ayuso, Sorption of Zn, Cd and Cr on calcite: application to purification of industrial wastewaters, Miner. Eng. 15 (2002) 539–547, https://doi.org/10.1016/s0892-6875(02)00072-9.
[78] A.K.V. Raj, P.P. Rao, T.S. Sreena, T.R.A. Thara, Broad greenish-yellow luminescence in $CaMoO_4$ by Si^{4+} acceptor doping as potential phosphors for white light emitting diode applications, J. Mater. Sci. Mater. Electron. 29 (2018) 16647–16653, https://doi.org/10.1007/s10854-018-9757-x.
[79] X. Liu, Z. Wang, Y. Niu, C. Liu, H. Chen, X. Ren, M. Wang, W.M. Lau, D. Zhou, Scalable synthesis of novel V_2O_3/carbon composite as advanced cathode material for aqueous zinc-ion batteries, Ceram. Int. 48 (2022) 15594–15602, https://doi.org/10.1016/j.ceramint.2022.02.093.
[80] K. Zhu, T. Wu, K. Huang, A high-voltage activated high-erformance cathode for aqueous Zn-ion batteries, Energy Storage Mater. 38 (2021) 473–481, https://doi.org/10.1016/j.ensm.2021.03.031.
[81] J. Huang, Z. Wang, M. Hou, X. Dong, Y. Liu, Y. Wang, Y. Xia, Polyaniline-intercalated manganese dioxide nanolayers as a high-performance cathode material for an aqueous zinc-ion battery, Nat. Commun. 9 (2018) 2906, https://doi.org/10.1038/s41467-018-04949-4.
[82] F. Ming, H. Liang, W. Zhang, J. Ming, Y. Lei, A.H. Emwas, H.N. Alshareef, Porous MXenes enable high performance potassium ion capacitors, Nano Energy 62 (2019) 853–860, https://doi.org/10.1016/j.nanoen.2019.06.013.
[83] Z. Zhang, B. Xi, X. Wang, X. Ma, W. Chen, J. Feng, S. Xiong, Oxygen defects engineering of $VO_2{\cdot}xH_2O$ nanosheets via *in situ* polypyrrole polymerization for efficient aqueous zinc ion storage, Adv. Funct. Mater. 31 (2021) 2103070, https://doi.org/10.1002/adfm.202103070.
[84] J. Meng, Y. Song, Z. Qin, Z. Wang, X. Mu, J. Wang, X.X. Liu, Cobalt–nickel double hydroxide toward mild aqueous zinc-ion batteries, Adv. Funct. Mater. 32 (2022) 2204026, https://doi.org/10.1002/adfm.202204026.
[85] S. Shen, D. Ma, K. Ouyang, Y. Chen, M. Yang, Y. Wang, S. Sun, H. Mi, L. Sun, C. He, An *in situ* electrochemical amorphization electrode enables high-power high-cryogenic capacity aqueous zinc-ion batteries, Adv. Funct. Mater. 33 (2023) 2304255, https://doi.org/10.1002/adfm.202304255.
[86] Z. Wang, Y. Song, J. Wang, Y. Lin, J. Meng, W. Cui, X.X. Liu, Vanadium oxides with amorphous-crystalline heterointerface network for aqueous zinc-ion batteries, Angew. Chem. Int. Ed. 135 (2023) e202216290, https://doi.org/10.1002/anie.202216290.
[87] Y. Liu, Q. Li, K. Ma, G. Yang, C. Wang, Graphene oxide wrapped CuV_2O_6 nanobelts as high-capacity and long-life cathode materials of aqueous zinc-ion batteries, ACS Nano 13 (2019) 12081–12089, https://doi.org/10.1021/acsnano.9b06484.
[88] S. Liu, H. Zhu, B. Zhang, G. Li, H. Zhu, Y. Ren, H. Geng, Y. Yang, Q. Liu, C.C. Li, Tuning the kinetics of zinc-ion insertion/extraction in V_2O_5 by *in situ* polyaniline intercalation enables improved aqueous zinc-ion storage performance, Adv. Mater. 32 (2020) e202216290, https://doi.org/10.1002/adma.202001113.
[89] Y. Zhu, C. Wang, Galvanostatic intermittent titration technique for phase-transformation electrodes, J. Phys. Chem. C 114 (2010) 2830–2841, https://doi.org/10.1021/jp9113333.
[90] G. Fang, C. Zhu, M. Chen, J. Zhou, B. Tang, X. Cao, X. Zheng, A. Pan, S. Liang, Suppressing manganese dissolution in potassium manganate with rich oxygen defects engaged high-energy-density and durable aqueous zinc-ion battery, Adv. Funct. Mater. 29 (2019) 1808375, https://doi.org/10.1002/adfm.201808375.
[91] T. Xiong, Z.G. Yu, H. Wu, Y. Du, Q. Xie, J. Chen, Y.W. Zhang, S.J. Pennycook, W.S. V. Lee, J. Xue, Defect engineering of oxygen-deficient manganese oxide to achieve high-performing aqueous zinc ion battery, Adv. Energy. Mater. 9 (2019) 1803815, https://doi.org/10.1002/aenm.201803815.
[92] Y. Huang, H. Yan, W. Liu, F. Kang, Transforming zinc-ion batteries with DTPA-Na: a synergistic SEI and CEI engineering approach for exceptional cycling stability and self-discharge inhibition, Angew. Chem. Int. Ed. (2024) e202409642, https://doi.org/10.1002/anie.202409642.